Climate response of fossil fuel and biofuel soot, accounting for soot's feedback to snow and sea ice albedo and emissivity

Mark Z. Jacobson

Department of Civil and Environmental Engineering, Stanford University, Stanford, California, USA

Received 22 April 2004; revised 5 July 2004; accepted 22 July 2004; published 6 November 2004.

[1] The first three-dimensional global model in which time-dependent spectral albedos and emissivities over snow and sea ice are predicted with a radiative transfer solution, rather than prescribed, is applied to study the climate response of fossil fuel plus biofuel black carbon plus organic matter (ff+bf BC+OM) when BC absorption in snow and sea ice is accounted for. The model treats the cycling of size-resolved BC+OM between emission and removal by dry deposition and precipitation from first principles. Particles produce and enter size-resolved clouds and precipitation by nucleation scavenging and aerosol-hydrometeor coagulation. Removal brings BC to the surface, where internally and externally mixed BC in snow and sea ice affects albedo and emissivity through radiative transfer. Climate response simulations were run with a ff+bf BC+OC emission inventory lower than that used in a previous study. The 10-year, globally averaged ff+bf BC+OM near-surface temperature response due to all feedbacks was about +0.27 K (+0.32 in the last 3 years), close to those from the previous study (5-year average of +0.3 K and fifth-year warming of +0.35 K) and its modeled range (+0.15 to +0.5 K) because warming due to soot absorption in snow and sea ice here (10-year average of +0.06 K with a modeled range of +0.03 to +0.11 K) offset reduced warming due to lower emission. BC was calculated to reduce snow and sea ice albedo by ~0.4% in the global average and 1% in the Northern Hemisphere. The globally averaged modeled BC concentration in snow and sea ice was ~5 ng/g; that in rainfall was ~22 ng/g. About 98% of BC removal from the atmosphere was due to precipitation; the rest was due to dry deposition. The results here support previous findings that controlling ff+bf BC+OM and CO_2 emission may slow global warming. *INDEX TERMS:* 0305 Atmospheric Composition and Structure: Aerosols and particles (0345, 4801); 0322 Atmospheric Composition and Structure: Constituent sources and sinks; 0368 Atmospheric Composition and Structure: Troposphere—constituent transport and chemistry; 1610 Global Change: Atmosphere (0315, 0325); *KEYWORDS:* climate change, black carbon, feedbacks, radiative effects, albedo, snow

Citation: Jacobson, M. Z. (2004), Climate response of fossil fuel and biofuel soot, accounting for soot's feedback to snow and sea ice albedo and emissivity, *J. Geophys. Res.*, *109*, D21201, doi:10.1029/2004JD004945.

1. Introduction

[2] Black carbon (BC), the main component of soot, directly warms the air by absorbing solar radiation, converting the solar radiation into internal energy (raising the temperature of the soot), and emitting, at the higher temperature, thermal-infrared radiation, which is absorbed selectively by air molecules. The warmer air molecules, which predominantly have long lifetimes, are transported to large scales, including to the global scale. The soot particles, which are removed within days to weeks by rainout, washout, and dry deposition, do not travel so far. Since the soot particles absorb solar radiation, they prevent that radiation from reaching the ground, cooling the ground immediately below them during the day. During the day and night, BC absorbs the Earth's thermal-infrared radiation, a portion of which is redirected back to the ground, warming the ground. In sum, soot particles create three major types of temperature gradients: (1) a daytime gradient in the immediate presence of soot where the atmosphere warms and the ground cools, (2) a nighttime gradient in the immediate presence of soot where the atmosphere warms and the ground warms, and (4) a large-scale daytime and nighttime gradient in the absence of soot but presence of advected air heated by soot where the atmosphere warms and the ground temperature is unchanged. In only one of these cases, which covers only a portion of the globe and only during the day, does soot cool the ground. These three types of temperature gradients set in motion feedbacks to meteorology, other aerosols, clouds, and radiation that affect temperatures further.

[3] When BC deposits to a surface, such as snow or sea ice, solar absorption and heating occur at the surface, so BC warms the surface directly. The heating due to BC at the surface melts some additional snow or sea ice, and the BC

0148-0227/04/2004JD004945$09.00

itself changes the reflectivity of snow. Both factors feed back to climate.

[4] Several studies to date have reported measurements of black carbon in snow or sea ice [e.g., *Warren*, 1982, 1984; *Clarke and Noone*, 1985; *Chylek et al.*, 1987; *Noone and Clarke*, 1988; *Warren and Clarke*, 1990; *Grenfell et al.*, 1994, 2002]. Other studies have modeled the albedo of snow containing BC inclusions [e.g., *Warren and Wiscombe*, 1980, 1985; *Chylek et al.*, 1983; *Warren*, 1984; *Aoki et al.*, 2000], the albedo of sea ice containing BC inclusions [*Light et al.*, 1998], and the optical properties of ice or snow containing other inclusions [e.g., *Higuchi and Nagoshi*, 1977; *Gribbon*, 1979; *Clark and Lucey*, 1984; *Woo and Dubreuil*, 1985; *Podgorny and Grenfell*, 1996]. A third set of studies has examined the effect on climate of pre-estimated albedo changes due to assumed changes of soot in snow [*Vogelmann et al.*, 1988; *Hansen and Nazarenko*, 2003]. Finally, several studies have modeled the effect of coated BC inclusions on aerosol optical properties [e.g., *Ackerman and Toon*, 1981; *Bohren*, 1986; *Chylek et al.*, 1995; *Jacobson*, 1997a, 1997b, 2000, 2001a; *Fuller et al.*, 1999; *Lesins et al.*, 2002], and at least two studies have measured the effect [*Chylek et al.*, 1988; *Schnaiter et al.*, 2003].

[5] *Warren and Wiscombe* [1980], for example, found that a concentration of 15 ng/g of soot in snow may be needed to reduce the albedo of snow by ~1%. *Light et al.* [1998] calculated that 150 ng/g of soot embedded in sea ice could decrease the spectral albedo of sea ice by up to 30%. *Twohy et al.* [1989] estimated that ~1000 times higher concentration of soot is needed for a cloud than for snow to cause the same albedo reduction because (1) snow optical thickness is much larger than is cloud optical thickness and (2) cloud drops are much smaller than ice crystals. For both reasons, light has more encounters with absorbing material in snow than in a cloud.

[6] In terms of global-scale effects, *Jacobson* [2002a] calculated a global warming due to fossil fuel black carbon and organic matter, excluding the effect of BC absorption in sea ice and snow, of +0.3 K averaged over 5 years and a fifth-year value of +0.35 K. The modeled range of warming from all simulations in that study was +0.15 to +0.5 K. *Hansen and Nazarenko* [2003] calculated, by prescribing changes in surface albedos, that BC absorption in snow and sea ice, alone, might be responsible for 0.17 K of the observed global warming to date.

[7] For this work, the global-scale climate response of soot from fossil fuel and biofuel sources is calculated from first principles, taking into account inclusions of soot in snow and sea ice. This work differs significantly from that of *Hansen and Nazarenko* [2003] in that this work treats the black carbon cycle (including size resolution) accounting for emission, transport, aerosol coagulation, aerosol growth, cloud activation, aerosol-cloud coagulation, cloud-cloud coagulation, rainout, washout, dry deposition, and processing of precipitated and dry-deposited BC in snow and sea ice. Second, snow and sea ice albedos and emissivities are predicted, not prescribed, here, accounting for calculated BC concentrations in snow and sea ice. Third, many climate feedbacks to size-resolved aerosols and size-resolved clouds, including the feedback of BC warming in snow and sea ice to melting, are accounted for here. In the paper by *Hansen and Nazarenko* [2003], snow and sea ice albedos were adjusted in advance, on the basis of estimated changes in albedo due to a set of observed BC concentrations in snow. Neither the black carbon cycle nor size-resolved aerosols nor size-resolved clouds were treated. Nevertheless, their study and the study of *Vogelmann et al.* [1988] provide some conceptual insight into the effects of changing snow and sea ice albedo due to BC, on climate. Below, the model used for this study, the specific treatment of soot inclusions in snow and sea ice, and results are discussed.

2. Treatment of BC Inclusions in Clouds, Precipitation, Snow, and Sea Ice

[8] The model used here is GATOR-GCMOM [*Jacobson*, 2001b, 2002a, 2002b, 2003], a parallelized and one-way-nested global-through-urban-scale Gas, Aerosol, Transport, Radiation, General Circulation, Mesoscale, and Ocean Model. The model has been compared with gas, aerosol, radiative, and meteorological data on regional and global scales [*Jacobson*, 1997b, 2001a, 2001b, 2001c, 2002a; *Jacobson et al.*, 2004]. Here, the model treated time-dependent gas, aerosol, radiative, dynamical, cloud, land surface, soil, and ocean processes over a 4°S-N × 5°W-E global grid and 39 sigma-pressure layers from the ground to 0.425 hPa (≈55 km), including 23 tropospheric layers and 4 layers below 1.3 km.

2.1. Atmospheric Dynamics and Transport Processes

[9] The global dynamical scheme is from *Arakawa and Lamb* [1981]. Transport of gases and aerosols is solved with the scheme of *Walcek and Aleksic* [1998] using online winds predicted by the dynamics modules and vertical diffusion coefficients predicted by the turbulence module (section 2.4).

2.2. Gas Processes

[10] Gas processes include emission, photochemistry (98 species; 202 reactions), advection, turbulence, cloud convection of gases, nucleation, condensation onto and dissolution into aerosols, clouds, and precipitation, washout, and dry deposition. Gases affect solar and thermal-IR radiation, aerosol formation, and cloud evolution, all of which feed back to meteorology.

2.3. Aerosol Processes

[11] Size-dependent aerosol processes include emission, homogeneous nucleation, condensation, dissolution, aerosol-aerosol coagulation, aerosol-cloud/ice/graupel coagulation, equilibrium hydration of liquid water, internal-particle chemical equilibrium, irreversible aqueous chemistry, evaporation of cloud drops back to aerosol-particles, transport, sedimentation, dry deposition, rainout, and washout. Aerosols in the model affect solar and thermal-IR radiation, cloud evolution, gas concentrations, and surface albedo and emissivities, all of which feed back to meteorology. The model size grid structure is the moving-center structure [*Jacobson*, 1997a]. The number concentration of particles and the mole concentrations of each component in each size distribution are prognostic variables. H_2SO_4-H_2O homogenous nucleation rates are calculated with the parameterization of *Vehkamaki et al.* [2002]. Homogeneous nucleation is

solved simultaneously with condensation of H_2SO_4-H_2O between the gas and all size bins with a mass-conserving, noniterative, and unconditionally stable scheme [*Jacobson*, 2002b], which is also used to condense organic gases onto size-resolved aerosols. The model treats dissolutional growth of NH_3, HNO_3, HCl, and soluble organics to all size bins with a mass-conserving, noniterative, and unconditionally stable dissolution scheme [*Jacobson*, 2002b]. Aerosol liquid water content, pH, and ion distributions in all bins are solved with EQUISOLV II [*Jacobson*, 1999]. Aerosol-aerosol coagulation is solved among all distributions and components and among total particles in each bin with a volume-conserving, noniterative, algorithm [*Jacobson*, 2002b].

2.4. Gas-Aerosol-Cloud-Turbulence Interactions

[12] Cumulus and stratus clouds form in the model by water growth onto size-resolved aerosol particles of different composition. The water available for growth is calculated as a function of height with stratus and cumulus parameterizations. The stratus cloud scheme is from *Mellor and Yamada* [1982] and is coupled with the calculation of turbulence (order 2.5). The stratus scheme predicts vertical cloud fraction and cloud water content in each layer given turbulence terms and vertical gradients in potential temperature and moisture. Turbulence parameters affect clouds, momentum, energy, and tracers, particularly in the boundary layer, which is resolved. Cumulus clouds are predicted with a modified Arakawa-Schubert algorithm [*Ding and Randall*, 1998]. In each column, nearly 500 subgrid cumulus clouds can form (and 1-10 typically form), each defined by a unique cloud base and top (when 23 layers exist below the tropopause, 22 bases and 22 tops are possible). For each subgrid cloud, water and energy transport are solved with a mass flux convection scheme; gas and size-resolved aerosol component transport are solved with a positive-definite, stable convective plume transport scheme. For each subgrid cloud, the model also generates cumulus precipitation, liquid water, ice, cumulus cloud fraction, and adjustments to large-scale potential temperature, momentum, and water vapor.

[13] Following convection, the bulk water predicted in each layer from the cumulus and stratus parameterizations is evaporated/sublimated, then regrown (simultaneously for liquid and ice) onto all aerosol sizes transported to that layer. The critical radius for liquid growth accounts for solutes within the aerosol particles and the Kelvin effect; that for ice growth accounts for the Kelvin effect. Because aerosols are transported vertically with cloud water, aerosol activation is consistent with that in a rising plume.

[14] Following growth, size-resolved processes treated include coagulation (liquid-liquid, liquid-ice, liquid-graupel, ice-ice, ice-graupel, and graupel-graupel, accounting for coagulation of aerosol components within hydrometeors), large drop breakup, settling, evaporative cooling during drop settling, evaporative freezing (freezing during drop cooling), heterogeneous and homogeneous freezing, contact freezing, melting, evaporation, sublimation release of aerosol cores upon evaporation/sublimation, coagulation of hydrometeors with interstitial aerosols, irreversible aqueous chemistry, gas washout, and lightning generation from size-resolved coagulation among ice hydrometeors. The coagulation kernel for all cloud processes includes a coalescence efficiency and collision kernels for Brownian motion, Brownian diffusion enhancement, turbulent inertial motion, turbulent shear, settling, thermophoresis, diffusiophoresis, and charge. These processes are described by *Jacobson* [2003]. Whereas *Jacobson* [2002a] treated the first indirect effect and part of the second indirect effect, the present work treats both the first and second indirect effects explicitly, on the basis of updates given by *Jacobson* [2003].

2.5. Radiative Processes

[15] Radiation calculations affect photolysis and heating. In each model column every hour, 676 irradiance and actinic flux calculations (84 UV+visible wavelengths $\times$ 1 probability interval each and 74 solar-IR+thermal-IR wavelengths $\times$ 8 probability intervals each) are calculated for each cloudy and clear sky, then weighted to give a grid cell average. The radiation solution scheme originates from *Toon et al.* [1989]. Solar-IR and thermal-IR gas absorption coefficients are parameterized for H_2O, CO_2, CH_4, CO, O_3, O_2, N_2O, CH_3Cl, $CFCl_3$, CF_2Cl_2, CCl_4 from HITRAN 2000 data to within 1% accuracy with a new method [*Jacobson*, 2004]. Aerosol particle optical properties assume that BC (if present) comprises a particle's core and all other material coats the core. Shell real and imaginary refractive indices for a given particle size and wavelength are obtained by calculating the solution-phase refractive index, calculating refractive indices of nonsolution, non-BC species, and volume averaging solution and nonsolution refractive indices [*Jacobson*, 2002b]. Core and shell refractive indices are used in a core shell Mie theory calculation [*Toon and Ackerman*, 1981]. Recently, *Schnaiter et al.* [2003] and M. Schnaiter (personal communication, 2004) found that the core shell theory works well at predicting absorption coefficients in comparison with experimental data as particles age because, as soot becomes coated by other material, its aggregate structure collapses closer to that of a sphere. Nevertheless, the core-shell technique is only approximate and may lead to some error in radiative calculations. Cloud liquid, ice, and graupel optical properties for each hydrometeor size and radiation wavelength in the model are also determined from Mie calculations. The radiative calculation accounts for topographical shading and atmospheric refraction. Spectral surface albedos and emissivities are calculated with the radiation code, as described in section 3.

2.6. Treatment of Subgrid Surface Temperatures and Oceans

[16] The model treats ground temperatures over subgrid surfaces (up to 12 soil classes and roads over soil, roofs over air, and water in each cell). It also treats vegetation over soil, snow over bare soil, snow over vegetation over soil, sea ice over water, and snow over sea ice over water [*Jacobson*, 2001b]. For all surfaces except sea ice and water, surface and subsurface temperatures and liquid water are found with a time-dependent 10-layer module. Global soil moisture is initialized with monthly gridded values from *Nijssen et al.* [2001] and global fractional vegetation cover is obtained from *Zeng et al.* [2000]. Sea

ice thickness is predicted with a time-dependent slab calculation. Ocean mixed-layer velocities, energy transport, and mass transport are calculated with a gridded two-dimensional (2-D) potential enstrophy, energy, and mass-conserving shallow-water equation module, forced by wind stress (G. Ketefian and M. Z. Jacobson, manuscript in preparation, 2004), based on the shallow-water scheme of *Arakawa and Lamb* [1981]. The actual depth at each location is a prognostic variable, but because the module conserves volume exactly, the average mixing depth over the global ocean is constant (80 m). For lake water, a fixed 80 m mixing depth is assumed. Water (ocean and lake) temperatures are also affected by sensible, latent, and radiative fluxes.

2.7. Emissions

[17] Anthropogenic gas and aerosol emissions were the same as those given by *Jacobson* [2002a] except as follows. *Jacobson* [2002a] used fossil fuel BC emissions from *Cooke et al.* [1999] (which totaled 5.1 Tg-C/yr), and multiplied this amount by 2.4 to obtain OC and by 3.1 to obtain OM (organic matter) emissions from fossil fuels. When removing BC, OM was removed in the ratio 2:1. The monthly biomass-burning BC inventory used in that paper was from *Cooke and Wilson* [1996] and totaled 6 Tg-C/yr. All biomass-burning gas and non-BC particle emissions in that paper were scaled to biomass-burning BC emissions in space and time.

[18] Here, an early version of the BC inventory from *Bond et al.* [2004] was used. In this version, submicron fossil fuel+biofuel (ff+bf) BC and OC emissions were 3.92 and 5.98 Tg-C/yr, respectively, and submicron biomass-burning BC and OC emissions were 3.14 and 25.6 Tg-C/yr, respectively. The submicron ff+bf BC and OM emission rates are lower than that from the most recent inventory values of *Bond et al.* [2004] (near 4.9 and 8.9 Tg-C/yr, respectively, with a range of uncertainty of 3.2–10.2 and 5.1–16.9 Tg-C/yr, respectively), and are about 20% and 60% lower than those used by *Jacobson* [2002a]. The most recent inventory of *Bond et al.* [2004] was not used for this study because the computer simulations, which required over 10 months of computer time, was substantially finished when the new inventory became available.

[19] Nevertheless, it was assumed here that supermicron BC and OC emissions were 25% and 45% of submicron BC and OC emissions, respectively, for both fossil fuels+biofuels and biomass burning [*Cooke and Wilson*, 1996]. Whereas, this estimate could be high for many sources, it put the total (all sizes) ff+bf BC and OC emissions at 4.9 and 8.7 Tg-C/yr, close to the mean submicron values of the most recent inventory.

[20] The organic matter:organic carbon (OM:OC) ratio of emitted organics in the present study was set to 1.6, the ambient urban value given by *Turpin and Lim* [2001]. The ratio for ambient aerosols may vary from 1.2 to 3.2, with an average for nonurban aerosols of 2.1 [*Turpin and Lim*, 2001], but since the OM:OC ratio needed here is for emission only, the urban value is most relevant.

[21] Finally, the yearly biomass-burning BC inventory of *Bond et al.* [2004] was distributed monthly by scaling it to the monthly inventory of *Cooke and Wilson* [1996]. Emission rates of other species emitted in biomass burning aside from BC and OM were calculated from the new monthly BC values in the same way as given by *Jacobson* [2002a]. When emitted BC was removed during sensitivity simulations, all OM was removed simultaneously.

3. Rainout and Washout of BC in Size-Resolved Precipitation

[22] In the model, BC enters clouds and precipitation in two ways. The equations representing these processes are given by *Jacobson* [2003]; here, the processes are described briefly.

[23] The first method is nucleation scavenging (which leads to rainout), whereby cloud liquid and ice grow directly onto size-distributed aerosol particles, some of which contain BC. This process conserves both the total number concentration of aerosol and the mass concentration of each aerosol component and the mass of water among the gas, liquid, and solid phases. Of the initial aerosol distribution present prior to nucleation scavenging, some particles are activated as liquid, some are activated as ice, and the rest are interstitial. The mass of BC incorporated in the size-resolved liquid and ice hydrometeors plus that in the interstitial aerosols is the same as the BC mass before cloud processing. Next, size-resolved coagulation transfers BC, other aerosol components, and water in hydrometeors to larger liquid or ice sizes by liquid-liquid and ice-ice coagulation and to larger sizes of the graupel distribution by ice-liquid, liquid-graupel, ice-graupel, and graupel-graupel coagulation. All coagulation equations are solved simultaneously among all distributions. If any hydrometeor particle coalesces to large enough size to overcome air viscosity, it falls below the cloud and begins to evaporate or sublimate. If it shrinks sufficiently so that it can no longer overcome viscosity, the hydrometeor stays suspended in air below the cloud. If it reaches the surface as precipitation, and the surface is snow or sea ice, the BC, which has a distinct size in each size-resolved hydrometeor, is added to a thin layer at the top of the snow or sea ice. Its subsequent evolution is discussed in section 4. BC that reaches the surface of the ocean is assumed to disappear into the ocean; that reaching soil, vegetation, a road, or a rooftop is assumed to blend in or be covered rapidly (in the case of sand). Ignoring BC that lands on these surfaces may result in a slight underestimate of the climate effects of BC.

[24] The second method that BC enters a cloud is by impaction scavenging (aerosol-hydrometeor coagulation), which leads to washout. This process is accounted for by allowing size-resolved interstitial aerosols containing BC to coagulate with then enter size-resolved liquid, ice, and graupel hydrometeors within or below the cloud. If the hydrometeor reaches a snow or sea ice surface, the BC is again added to the surface.

[25] Additional interactions affect the distribution of BC in clouds and precipitation. Contact freezing and homogeneous/heterogeneous freezing of liquid drops and their aerosol components move these constituents to the graupel distribution. Melting moves ice and graupel and their aerosol components to the liquid distribution. When large liquid drops break up, their water and aerosol constituents are distributed to smaller drops. Hydrometeor particles that evaporate below cloud before reaching the surface

release their aerosol particle cores, some of which deposit eventually by dry deposition.

4. BC Inclusions in Snow and Sea Ice

[26] BC in the model enters snow by precipitation and dry deposition. Its concentration in snow is also affected by changes in snow depth due to melting, vapor deposition, and sublimation. Precipitation falling to the surface includes size-resolved liquid, ice, and graupel. Aerosol components are carried to the surface in each size bin of each hydrometeor type. At the surface, snow and graupel are aggregated into one effective size bin for radiative calculations (r_{sn} = 150 μm), which is in the range of typical effective radii used for snow optical calculations [e.g., *Grenfell et al.*, 1994; *Aoki et al.*, 2000] and was chosen here on the basis of a best fit of modeled to measured spectral albedo, discussed in section 5. The calculation of dry deposition to snow and sea ice accounts for aerodynamic resistance, resistance to molecular diffusion, and the fall speed of particles [*Jacobson*, 1999, equation 20.11].

[27] To account for radiative effects of BC in snow, one snow layer is added to the bottom of each atmospheric model column (which otherwise extends from the surface to 55 km) for radiative calculations. The wavelength-dependent upward divided by downward irradiance at the top of this layer is the calculated surface solar albedo (0.165 to 10 μm). The wavelength-dependent emissivity, used for spectral thermal-IR calculations (3–1000 μm), is one minus the calculated albedo. As such, the model predicts (instead of prescribes) the changes in the albedo and emissivity of snow (and sea ice) each radiative time step, and these change are affected by aerosol inclusions within these surfaces and by atmospheric optical properties. Because changes in albedo and emissivity affect incident solar radiation and heating, such changes affect the melting of snow, which feeds back to soil moisture, albedo, and other climate variables.

[28] Snow depth (D_s, cm) in the model is affected by precipitation and melting [*Jacobson*, 2001b, equation (36)] as well as sublimation/ice deposition (added subsequently). For the radiative calculation through snow containing BC, the radiative snow layer thickness ($D_{s,r}$, cm) is assumed to be the smaller of the actual snow depth (D_s) and 10 cm. If $D_s \leq 10$ cm, the albedo/emissivity below this thin layer, needed as a boundary condition for the radiative calculation, is set to that of the underlying surface (sea ice, soil, vegetation, asphalt, or roofing material). If $D_s > 10$ cm, the radiative model bottom is still set to 10 cm below the snow surface, and the albedo at 10 cm depth is assumed to be that of pure snow, taken as a function of wavelength from *Grenfell et al.* [1994] for the solar spectrum and Z. Wan (MODIS UCSB emissivity library, www.icess.ucsb.edu/modis/EMIS/html/em.html, 1999) for the thermal-IR. The 10-cm limit for the snow layer was chosen since, from radiative calculations, only ~1% of light penetrates through this depth. Because of this, the selection of albedo at the bottom of the snow layer has little effect on the prediction of albedo at the layer top, as demonstrated by several tests here.

[29] Within each snow layer, it is necessary to calculate the concentration of BC. The time-dependent BC in snow (moles-BC cm^{-3}-snow) is calculated primarily as the sum of the concentrations due to precipitation and dry deposition: $c_{s,B,t} = c_{s,p,BC,t} + c_{s,d,BC,t}$. The time-dependent contribution from precipitation is

$$c_{s,p,BC,t} = c_{s,p,BC,t-h}\left(\frac{D_{s,r,t} - P_{s,t}h}{D_{s,r,t}}\right) + \frac{F_{p,BC,t}}{P_{s,t}h}\left(\frac{P_{s,t}h}{D_{s,r,t}}\right), \quad (1)$$

and that from dry deposition is

$$c_{s,d,BC,t} = \frac{c_{s,d,BC,t-h} + hF_{d,BC,t}/D_{s,r,t}}{1 + hS_{f,BC}/D_{s,r,t}}. \quad (2)$$

In these equations, t is the current time, h is the time step (s) for radiative calculations, $P_{s,t}$ is the snowfall rate, summed over all precipitation size bins ($cm^3\ cm^{-2}\ s^{-1}$ = cm s^{-1}), $F_{p,BC,t}$ is the flux of BC to the surface, summed over all precipitation bins (moles $cm^{-2}\ s^{-1}$), $F_{d,BC,t}$ is the dry-deposition flux of BC to the surface, summed over all aerosol bins, and accounts for gravitational settling of BC onto and impaction of BC with snow (moles $cm^{-2}\ s^{-1}$), and $S_{f,BC}$ is the fall speed of dry-deposited BC through the top snow layer to below the layer (cm s^{-1}).

[30] Equation (1) assumes that, each time step, new snow of depth $P_{s,t}h$(cm), containing BC mole concentration $F_{p,BC,t}/P_{s,t}h$(moles-BC/cm^3 −snow) is added to the top of the radiative snow layer of depth $D_{s,r,t}$, and BC in the concentration $c_{s,p,BC,t-h}$(moles-BC/cm^3 −snow) is removed from the bottom $P_{s,t}h$ cm of the layer. In this manner, the thickness of the radiative snow layer stays constant unless $D_{s,r,t} < 10$ cm, in which case BC is not removed from the bottom.

[31] When snow sublimates, the total snow depth, D_s, and the radiative layer depth, $D_{s,r,t}$, both decrease by an amount $D_{sub,t}$. If, after sublimation, $D_s > 10$ cm, then $D_{s,r,t}$ must remain at 10 cm by adding snow of depth $D_{sub,t}$ to the bottom of the radiative layer. With the assumption that the BC concentration below the radiative layer is the same as that in the layer, the average concentration of BC in the radiative layer after depth $D_{sub,t}$ is added back to its bottom, is $c_{s,p,BC,t} = c_{s,p,BC,t}\ (1 + D_{sub,t}/D_{s,r,t})$, which allows BC to build up in concentration during sublimation. When $D_s \leq 10$ m, the radiative layer only shrinks, and the BC concentration is instead adjusted by $c_{s,p,BC,t} = c_{s,p,BC,t}D_{s,r,t}/(D_{s,r,t} - D_{sub,t})$, except that no further increase is allowed when $D_{s,r,t} < 2$ cm. When snow increases by depth $D_{dep,t}$ due to ice deposition, the concentration of BC in snow decreases by $c_{s,p,BC,t} = c_{s,p,BC,t}\ (1 - D_{dep,t}/D_{s,r,t})$ when $D_s > 10$ cm and by $c_{s,p,BC,t} = c_{s,p,BC,t}D_{s,r,t}/(D_{s,r,t} + D_{dep,t})$ when $D_s \leq 10$ cm. When melting occurs, drainage of BC through the snow is assumed to compensate for the increase in concentration of BC due to the reduction in the snow water content. In future studies, the drainage of BC originating from precipitation during a melt should be modeled in a manner similar to the drainage of BC originating from dry deposition (equation (2)).

[32] The precipitation flux of snow ($P_{s,t}$) and the precipitation flux of BC ($F_{p,BC,t}$) to snow are predicted in the model (section 3) since BC exists in each size bin in each hydrometeor type falling to the surface. The fluxes of individual aerosol components within each size of each type of precipitation (liquid, ice, graupel) are solved together with the flux of the precipitation itself. The BC precipitation flux in snow is then aggregated over all size bins of ice and graupel to give $F_{p,BC,t}$.

[33] The fall speed of dry-deposited BC through snow is a function of particle size and composition. Studies have shown that very large (>600 μm) dirt particles sink through the snow; particles from 1 to 600 μm tend to aggregate on the snow, and submicron particles, particularly if they are hydrophilic, are flushed through the snow with meltwater [e.g., *Rhodes et al.*, 1987; *Conway et al.*, 1996]. *Conway et al.* [1996], for example, found that 50% of the mass of hydrophobic soot and 99% of hydrophilic soot passed through 50 cm of snow in 10 days during July and August on Blue Glacier. These numbers give the *e*-folding lifetime of hydrophobic and hydrophilic soot through a 50-cm layer of snow as $\tau_{s,BC}$ = 14.4 and 2.17 days, respectively, and a fall speed of soot through snow ($S_{f,BC} = D_{s,r,t}/\tau_{s,BC}$) of 3.5 and 23 cm/day ($4 \times 10^{-5}$ to 2.7×10^{-4} cm s^{-1}), respectively. To account for times of the year when snow is not melting so readily, the fall speed of dry-deposited soot through snow used here was set to a relatively small value $S_{f,BC} = 10^{-5}$ cm s^{-1}, although much variation exists. Because precipitation is responsible for >97% of BC deposited to snow (found here), and the fall speed calculation is not necessary for precipitated snow (see equation (1)), the uncertainty in the fall speed of dry-deposited BC through snow, $S_{f,BC}$, is unlikely to affect the main conclusions here.

[34] For snow BC optical calculations, BC is treated as partly internally mixed as a core within snow grains and partly externally mixed from snow grains (in both cases, the BC may still be internally mixed with other aerosol constituents). The refractive index of BC is taken from *Krekov* [1993]. The density of emitted soot aggregates varies as a function of diameter and soot composition from 0.2–2.25 g/cm^3 [e.g., *Fuller et al.*, 1999; *Maricq et al.*, 2000]. The value 1.5 g/cm^3 is chosen for this study because it is relatively consistent with the mean size of emitted soot from *Maricq et al.* [2000, Figure 5], although no single number captures the density of soot.

[35] The total concentration of BC in snow in the model is $c_{s,BC,t}$. In the case of precipitated snow, each snow grain is ideally assumed to contain multiple BC inclusions. However, for global 3-D calculations, it is feasible at this time only to treat one internally mixed inclusion per grain, multiple externally mixed inclusions per grain, or both. If all BC is assumed to be one internally mixed inclusion, the BC inclusion radius can become unrealistically large, particularly in the case of sea ice. For example, for a 2.5 mm radius sea ice grain with a value of 25 ng-BC/g-ice, a sea ice density of 0.5 g/cm^3 and a BC density of ρ_{BC} = 1.5 g/cm^3, a single BC inclusion has a radius of 8.86 μm, which is unrealistic.

[36] In reality, BC is emitted in particles primarily near 15–80 nm radii. As BC ages, though, its mean size increases because of coagulation only (condensation affects the mean size of particles containing BC but not of the BC itself). Here, it is assumed for snow and sea ice radiative calculations, that the mean radius of BC itself (not of aerosol particles containing BC) is r_{BC} = 133 nm for snow and sea ice optical calculations when BC is a core in a snow/sea ice grain and when BC is externally mixed from snow and sea ice (but still internally mixed with other aerosol constituents in both cases). Although, in reality the radius of BC itself within aerosol particles varies, and although the model provides BC as a function of size within precipitating snow and dry-depositing aerosols, BC was agglomerated simply to save computer time. The error of assuming a single radius for BC within snow should not be large because at smaller sizes, for example, the decrease in absorption efficiency is largely offset by the increase in cross-sectional area concentration. To illustrate, the reduction in albedo at 550 nm due to 25 ng/g of BC at a radius of 133 nm is ~2.3% (section 5) whereas that due to 25 ng/g of BC at a radius of 45 nm (an unrealistically low mean radius for aged particles), is 2.8%. Using the model of *Warren and Wiscombe* [1980], *Clarke and Noone* [1985] found that the addition of 25 ng/g of soot to snow decreased snow albedo by ~2.0%, close to the value obtained with the 133 nm radius.

[37] In the case of snow, the mole concentration of BC externally mixed from snow grains is calculated as $c_{s,EM,BC,t} = c_{s,BC,t} - c_{s,IM,BC,t}$, where

$$c_{s,IM,BC,t} = \min\left(\frac{r_{BC}^3}{r_{sn}^3}\frac{\rho_{BC}}{m_{BC}} D_{s,r,t}, c_{s,BC,t}\right) \tag{3}$$

(moles-BC cm^{-3}-snow) is the concentration of BC internally mixed within snow grains. In this equation, m_{BC} is the molecular weight of carbon (12.01 g mole^{-1}).

[38] The total scattering optical depth through the snow radiative layer is then

$$\tau_{s,sn,\lambda} = Q_{s,r_{sn}\lambda,ic-BC} D_{s,r,t} n_{sn} \pi r_{sn}^2 + Q_{s,r_{BC}\lambda,BC} D_{s,r,t} n_{s,EM,BC,t} \pi r_{BC}^2, \tag{4}$$

where $Q_{s,r_{sn}}\lambda,ic-BC$ and $Q_{s,r_{BC}}\lambda,BC$ are the wavelength-dependent single-particle scattering efficiencies of ice at grain size r_{sn} with a BC core and of BC externally mixed from snow at size r_{BC}, respectively. In addition,

$$n_{sn} = \frac{3}{4\pi r_{sn}^3}\frac{\rho_{sn}}{\rho_{ic}} \tag{5}$$

is the number concentration of snow grains (grains cm^{-3}) at the radius of a pure ice grain (the Mie calculation uses the indices of refraction of pure ice) [e.g., *Light et al.*, 1998], and

$$n_{s,EM,BC,t} = \frac{c_{s,EM,BC,t}}{4\pi r_{BC}^3/3}\frac{m_{BC}}{\rho_{BC}} \tag{6}$$

is the number concentration (particles cm^{-3}) of externally mixed BC particles. In equation (5), ρ_{sn} is the density of new snow (assumed to be 0.2 g cm^{-3}, which is in the range of 0.12–0.33 g cm^{-3} from [*Aoki et al.*, 2000]), ρ_{ic} is the density of pure ice (temperature dependent and 0.9167 g cm^{-3} at 0°C). Absorption and forward scattering optical depths have expressions similar to equation (4), but with single-particle absorption and forward scattering efficiencies, respectively, instead of total scattering efficiencies.

[39] Because BC externally mixed from snow (but internally within aerosol particles) is surrounded by snow grains that are highly scattering, absorption by such externally mixed BC is enhanced in a manner similar to that of a BC core within a single grain. As such, the treatment of multiple

BC particles as externally mixed within snow appears, to first order, to be similar to treating multiple BC inclusions within individual grains.

[40] Optical depths of sea ice with BC inclusions are calculated in a manner similar to those of snow with BC inclusions, except that the sea ice grain radius is assumed to be r_{si} = 2.5 mm, the sea ice density is assumed to be ρ_{si} = 0.5 g cm^{-3} [*Light et al.*, 1998], and the spectral albedo at the bottom of the sea ice surface is assumed to be ~60% of that of snow. The concentration of BC in sea ice is calculated with equations (1) and (2), except that if sea ice contains more than 1 cm of snow on its top, the radiative layer is assumed to be a snow layer.

5. Modeled Versus Measured Spectral Albedos

[41] Figure 1a compares modeled with measured spectral albedos over a pure snow surface for two different assumed radii of snow crystals. The model calculation was from a 1-D radiative transfer calculation through a 39-layer atmosphere and a 10-cm layer of snow at the bottom, assuming a zenith angle of 72° and no impurities in the snow. The albedo was calculated as the upward divided by downward irradiance at the top of the snow layer. The data were averages of South Pole and Vostok data from *Grenfell et al.* [1994, Table 6], interpolated to the model wavelength intervals. The comparison suggests that between 0.2 and 0.7 μm wavelength, grain sizes of r = 150 μm and r = 60 μm gave nearly identical albedos, and both grain sizes matched the data well. From 0.7 to 1.5 μm wavelength, a grain size of r = 150 μm gave almost an exact fit to the observed albedo. Above 1.5 μm wavelength, r = 60 μm gave a better fit. The fit at higher wavelengths, in both cases, could be improved by using a higher-resolution model wavelength grid (only 5 wavelengths were used between 1.5 and 2.5 μm). However, it was desired to use the actual wavelength grid used in the 3-D model for the comparison. Since most energy of the solar spectrum lies below 1.5 μm wavelength, r = 150 μm was used here for the 3-D simulations.

[42] Figure 1b compares modeled (from radiative transfer) spectral albedos over snow when r = 150 μm but at different zenith angles (θ = 55° and 72°) and over sea ice at a single zenith angle but with different assumed grain sizes (2.5 and 10 mm). The results show that increasing grain size decreases albedo, as expected. The 2.5 mm grain size is used here for sea ice.

[43] Figures 1c and 1d compare modeled spectral albedos over snow and sea ice, respectively, containing different BC mass mixing ratios when each snow grain contains a single internally mixed BC inclusion and the rest of the BC in snow is assumed to be externally mixed from snow or sea ice grains (all BC particles in snow were assumed to be 266 nm in diameter). The results suggest that 25 ng/g of BC might reduce the albedo of snow at 550 nm by 2.3% and of sea ice at 550 nm by 2.1%. As discussed earlier, *Clarke and Noone* [1985] similarly found that the addition of 25 ng/g of soot to snow decreased snow albedo by ~2.0%. Figure 1d here shows that the addition of 5 ng/g and 100 ng/g of BC to sea ice might reduce its 550 nm albedo by 0.43% and 7.6%, respectively. The modeled effect of BC on emissivity is small. For example, at wavelength 7.75 μm, an increase from 0 to 500 ng/g BC increases emissivity by only 0.0005%.

[44] Although snow grain size varies with meteorological conditions, age of snow, and depth [e.g., *Massom et al.*, 2001], Figure 1a shows that the difference in albedo due to two different grain radii (60 and 150 μm) is relatively small. Further, a comparison of model versus zonally averaged albedo (Figure 8) shows that the choice of r = 150 μm grain size appears reasonable. Finally, this study examines the difference in climate response due to the presence versus absence of BC. Although the absolute albedo differs slightly at different snow grain sizes (Figure 1a), the change in albedo due to the addition of a given mixing ratio of BC is similar to that at another grain size. For example, Figure 1e shows the albedo difference due to adding 25 ng/g of BC to snow at 60 μm grain size minus that due to adding 25 ng/g of BC to snow at 150 μm grain size. The largest albedo difference in the figure is 0.006. Thus the choice of grain size, which affects the absolute albedo to some degree, has relatively little effect on the albedo difference arising because of the addition of BC to snow or sea ice.

6. Analysis of 3-D Results

[45] Four 10-year simulations were run. The first two were with and without, respectively, ff+bf BC+OM emission, when BC absorption in sea ice and snow was treated in both cases (''baseline absorption'' and ''sensitivity absorption'' cases, respectively). The second two were with without, respectively, ff+bf BC+OM emission when BC absorption in sea ice or snow was not treated in either case (''baseline no absorption'' and ''sensitivity no absorption'' cases, respectively). All four cases included biomass-burning (bb) BC+OM emission, emission of all other species, and treatment of all other processes previously described.

[46] Figure 2a shows the 10-year average modeled near-surface BC concentration in air (μg m^{-3}), accounting for all BC sources (ff+bf+bb), in the baseline absorption case. This figure shows a higher concentration of BC in India and a lower concentration in Europe than given by *Jacobson* [2002a, Figure 2] because the emission inventory here includes BC biofuel emissions whereas the previous inventory did not. Also, BC emissions in Europe are lower in the present inventory than in the previous inventory. Concentrations of BC were greatest over land but small concentrations of BC penetrated globally, particularly in elevated layers (not seen in the figure). Figure 2b shows the ff+bf contribution to the 10-year-averaged BC concentration in Figure 2a, obtained by taking the difference in BC between the baseline and sensitivity simulations in the absorption case.

[47] Tables 1 and 2 compare baseline-modeled with measured BC in snow/sea ice and rainwater, respectively. At several locations (e.g., Alert, Greenland Sea, Spitzbergen, Barrow), modeled BC in snow/sea ice was lower than that observed. At other locations (e.g., Hurricane Hill, South Pole, Greenland, Halifax, Arctic Ocean), modeled values were close to those measured. Since modeled BC concentrations in snow were lower in some locations than those measured, it is possible that the BC warming found here due to snow/sea ice absorption is somewhat underestimated. On the other hand, many of the underestimated measurements

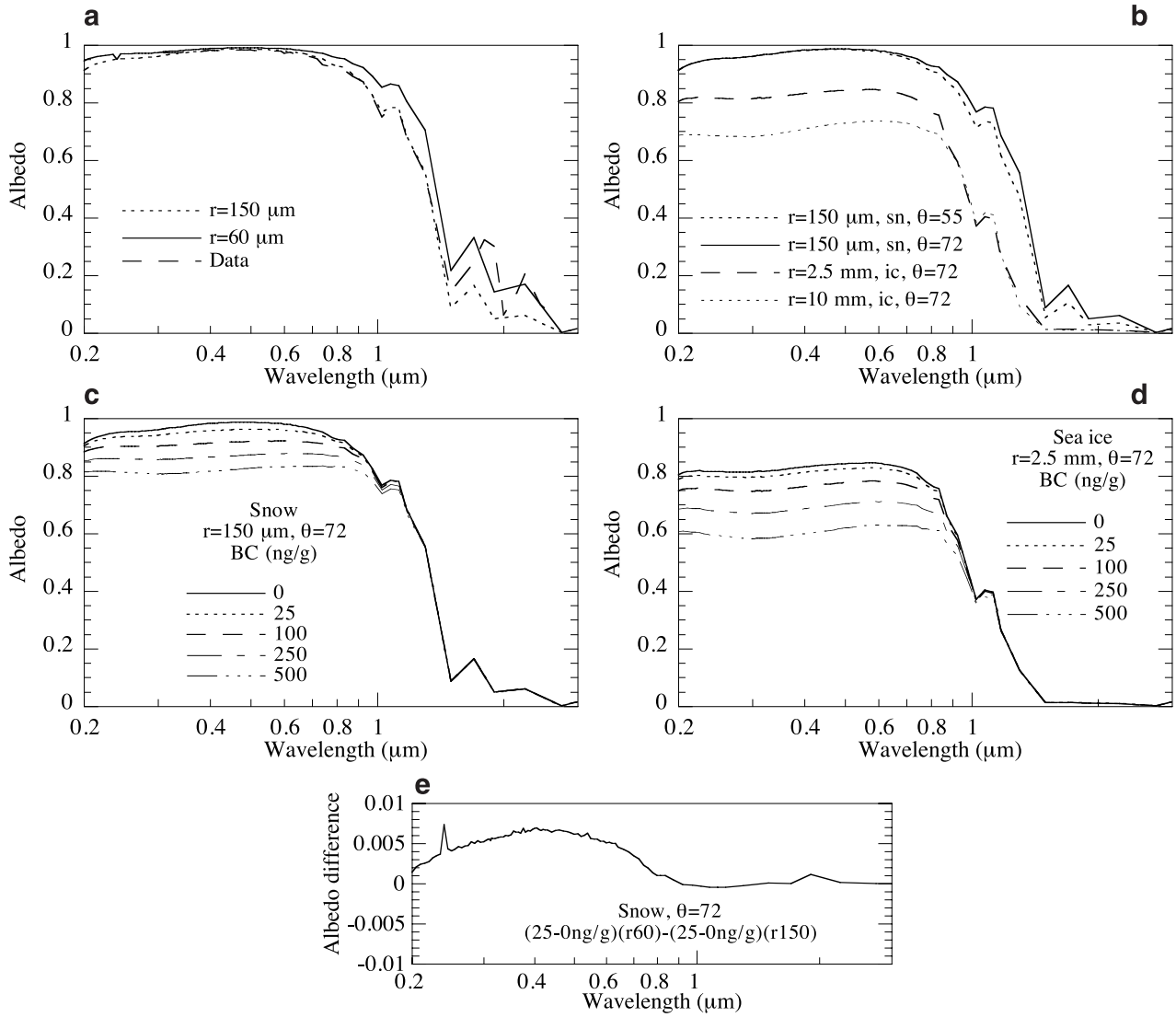

Figure 1. (a) Comparison of modeled with measured spectral albedos over a pure snow surface for different assumed radii of snow crystals. The model calculation was from a 1-D radiative transfer calculation through a 39-layer atmosphere and a 10-cm layer of snow at the bottom, assuming a zenith angle of 72° and no impurities in the snow. The albedo was calculated as the upward divided by downward irradiance at the top of the snow layer. The data were an average of South Pole and Vostok data from *Grenfell et al.* [1994, Table 6], interpolated to the model wavelength intervals. (b) Comparison of modeled (from radiative transfer) spectral albedos over snow with a single grain radius (150 μm) but at different zenith angles (θ = 55° and 72°) and over sea ice at a single zenith angle but with different assumed grain sizes (2.5 and 10 mm). (c) Comparison of modeled spectral albedos over snow containing different BC mass mixing ratios when each snow grain contains a single internally mixed BC inclusion and the rest of the BC in snow is assumed to be externally mixed (all BC particles in snow are assumed to be 266-nm diameter). (d) Same as Figure 1c, but for sea ice. (e) Albedo difference due to adding 25 ng/g of BC to snow at 60-μm grain size minus that due to adding 25 ng/g of BC to snow at 150-μm size.

were made in the 1980s, so they may no longer be applicable, particularly since the emission inventory for BC was derived for 1996. The model matched the most recent measurements the best. Model predictions of BC in rainwater were also rarely overestimated. In some cases (north Sweden, Mace Head, Gif sur Yvette), they were underestimated noticeably. Again, many of rainwater measurements were made in the 1980s whereas the emission inventory used here was for 1996.

[48] The mass-scavenging ratio of BC due to snowfall is the mass mixing ratio of BC in snowmelt (μg-BC/g-meltwater) divided by that in air (μg-BC/g-air). The time-averaged scavenging ratio for BC over all snow surfaces globally was calculated here as ~125, which compares with 180 ± 120 for sulfate at an individual location over time from *Davidson et al.* [1985]; 160 for BC at several locations from *Clarke and Noone* [1985], and 97 ± 34 for BC at several locations from *Noone and Clarke* [1988].

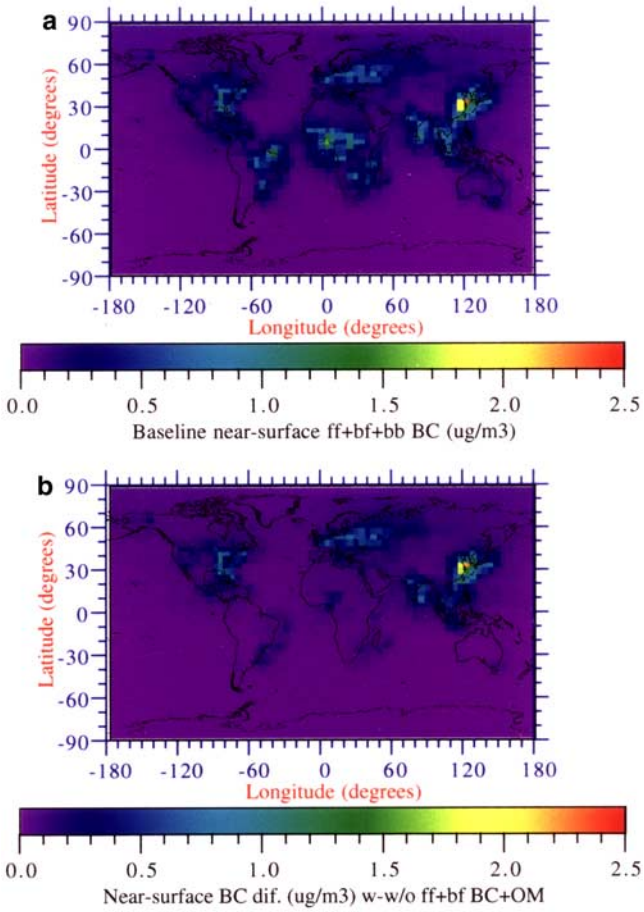

Figure 2. (a) Ten-year-averaged baseline near-surface modeled BC concentration ($\mu g\ m^{-3}$), accounting for fossil fuel plus biofuel plus biomass-burning (ff+bf+bb) emission. (b) Ten-year difference in near-surface BC concentration ($\mu g\ m^{-3}$) when ff+bf BC+OM emission was versus was not included in the calculation ("baseline absorption" minus "sensitivity absorption" cases). Snow/sea ice absorption by BC was accounted for in both panels.

[49] The modeled average concentration of BC in snow and sea ice globally was 5 ng/g. About 98% of the average concentration was due to precipitation and the rest was due to dry deposition. The maximum instantaneous BC concentration in snow or ice anywhere was 120 ng/g. The modeled globally averaged concentration of BC in rain was 22 ng/g with a maximum instantaneous value anywhere of 640 ng/g.

[50] Figure 3a shows the 10-year-averaged global temperature difference between the baseline and sensitivity calculation in the snow/ice absorption case, and Figure 3b shows the difference in the no-absorption case. The two figures represent the effect of ff+bf BC+OM emission on global temperatures, but when BC absorption by snow and sea ice was and was not included, respectively. In both figures, ff+bf BC+OM emission warmed eastern Europe and western and central Russia. In the absence of snow/sea ice absorption (Figure 3b), ff+bf BC+OM caused cooling over the Greenland Sea, some of which contained sea ice covered by snow. With absorption, much of that cooling turned to warming. The figure does not account for any change in CO_2. The difference between Figures 3a and 3b suggests that BC absorption in snow and sea ice had the greatest atmospheric warming effect in and around the Greenland Sea. Some cooling occurred over Alaska and the Arctic between Alaska and Russia. This may have been due to a feedback to large-scale meteorology (e.g., large-scale feedbacks to pressure, winds, and humidity due to BC). Figure 4, for example, shows the difference in air pressure and winds between the two simulations in which ff+bf BC+OM emission was included in both cases but absorption by snow and sea ice were and were not included, respectively. The figure shows that allowing BC absorption in snow and sea ice triggered changes in pressure and winds globally. These changes may have been a cause of or response to changes in temperature or both.

[51] Although Figures 3a and 3b were generated from four independent simulations, each under slightly different conditions, and even though the model calculation in all cases included feedbacks among gases, aerosols, clouds, radiation, atmospheric dynamics, ocean dynamics, and soil processes, there is little random, as opposed to expected, variation between the two figures. The differences between Figures 3a and 3b occur in areas where differences are expected: where sea ice and/or snow are present. If model random variability were an important factor affecting the results, one might expect ff+bf BC+OM warming to occur in different locations, such as in Africa instead of eastern Europe, between Figures 3a and 3b. Since the figures are relatively consistent except for the expected result of differential cooling/warming due to BC absorption in snow/sea ice, it can be hypothesized that random variability of model results may not have a significant effect on the conclusions of this study.

[52] Figure 5a shows the vertical profile of the 10-year and globally averaged layer and cumulative temperature differences in the absorption case. For this and other temperature calculations, the layer temperature is defined as

$$T_k = \frac{\sum_{i,j,t} V_{i,j,k,t}\rho_{a,i,j,k,t}c_{p,a}T_{i,j,k,t}}{\sum_{i,j,t} V_{i,j,k,t}\rho_{a,i,j,k,t}c_{p,a}}, \tag{7}$$

where the sums are over all grid cells i and j in the layer k and over all time steps t during the averaging period, $V_{i,j,k,t}$ is the volume of a grid cell at a given time step and location, $\rho_{a,i,j,k,t}$ is the density of moist air (dry air plus water vapor) in a cell at a given time step, $c_{p,a}$ is the specific heat of moist air at constant pressure, and $T_{i,j,k,t}$ is the temperature in a cell. Figure 5a shows the layer temperature difference between two simulations. The lowest layer temperature difference is the ground temperature difference. The cumulative temperature from one simulation is the integrated layer temperature from the first air layer (not the ground) adjacent to the surface ($m = 1$) to the layer of interest (k):

$$T_{c,k} = \sum_{m=1}^{k} T_m. \tag{8}$$

Layer temperatures in the stratosphere have little effect on cumulative temperature because air density is so low in the stratosphere that a large temperature change contributes little to total energy in the stratosphere.

Table 1. Comparison of Modeled and Measured BC in Snow or Sea Ice From the Baseline Absorption Case

Station	Latitude	Longitude	Modeled BC in Snow, ng/g	Measured BC in Snow/Sea Ice, ng/g	Period
Alert	83°30′N	62°30′W	1–2	45.5 (0–127)[a]	Nov.–Dec.
Greenland Sea	79°45′N	4°14′W	4–6	38.7 (5.4–75.5)[a]	July
Spitzbergen	79°N	12°E	5–7	31 (6.7–52)[a]	May
Barrow	71°18′N	156°36′W	3–6	23 (7.3–60.4)[a]	March–April
Abisko	68°18′N	18°30′E	15–26	33 (8.8–77)[a]	March–April
Hurricane Hill	48°00′N	123°30′W	14–32	14.7 (10.1–18.5)[a]	April
Arctic	65°–85°N	25°E to 160°W	2–35	25 (1.2–258)[a]	year
West Texas/New Mexico	32°N	106°W	14–24	2.2–25[b]	Dec.–April
Greenland			1–3	1.1–2.6[b]	Dec.–April
Antarctica			0.1–0.3	2.5[b]	Dec.–April
South Pole	90°S		0.1–0.2	0.2 (0.1–0.34)[c]	Jan./Feb.
Halifax, Nova Scotia	44°23′N	63°22′W	9–13	11 (4.3–32)[d]	Jan.–March
Arctic Ocean	76°N	165°E	3–4	4.4 (1–9)[d]	March–April

[a] *Clarke and Noone* [1985].
[b] *Chylek et al.* [1987].
[c] *Warren and Clarke* [1990] and *Chylek et al.* [1999].
[d] *Grenfell et al.* [2002].

[53] The figure shows that the temperature increase at the ground was ~0.20 K, increasing to 0.27 K at 140 m when ff+bf BC+OM emission and absorption were accounted for. The peak temperature increase occurred at around 300 hPa. At heights above 100 hPa, ff+bf BC+OM had relatively little effect on temperatures.

[54] Although the ground cooled relative to the atmosphere in the global average, the ground, averaged globally, experienced a net warming when BC was present for several reasons. First, as described in the introduction, soot creates three major types of temperature gradients: (1) warmer air, cooler ground locally during the day; (2) warmer air, warmer ground locally during the day; and (3) warmer air, neutral ground on the large scale during the day and night. In only one of these cases, which covers only a portion of the globe, does the ground cool. Over most of the globe and at night everywhere, soot warms the air but does not cool the ground. On the basis of this conceptual model, the net effect of soot should be to warm the air and, to a lesser extent, the ground, in the global average. Second, several feedbacks of soot enhance the warming of the ground following the warming of the air. For example, when the air warms during the day, the warming may reduce cloud cover, increasing solar radiation to the ground. Similarly, when the air warms relative to the ground during the day, the vertical transfer of horizontal momentum slows down, slowing winds near the surface, reducing emission of sea spray, soil dust, and road dust, warming the surface since these particles enhance scattering and the first indirect effect. The slower winds also reduce evaporation near the surface, warming the surface. Although the air warmed and the surface warmed to a lesser extent in the global average, the air and ground cooled in some regions (Figure 3) and the ground warmed more than the atmosphere in others.

[55] The net increase in surface temperature caused a net increase in evaporation on the global average (Figure 5c), but less than if the surface warmed to the same extent as the atmosphere. Although the first indirect effect (both the first and second were accounted for here) increased backscattering of incoming radiation to space in the presence of ff+bf BC+OM (Figure 5d), that effect was insufficient to counterbalance the direct daytime and nighttime warming of BC coupled with the warming due to the increase in water vapor, the increase in downward thermal-IR due to clouds with longer lifetimes, and feedbacks. The feedbacks treated are discussed in more detail by *Jacobson* [2002a].

[56] Figure 6 shows the portion of the vertical temperature difference in Figure 5a due to BC absorption in snow and sea ice. The figure was generated by taking the difference between the "baseline absorption" and "baseline no absorption" cases. The figure shows that BC absorption in snow/ice caused ~0.057 K (21%) of the 10-year-averaged ff+bf BC+OM near-surface warming and 0.04 K (20%) of the 10-year-averaged ground warming. The near-surface effect found here (near +0.06 K) is consistent in sign with but lower in magnitude than that of *Hansen and Nazarenko* [2003], who found a warming due to a pre-

Table 2. Comparison of Modeled and Measured BC in Rainwater From the Baseline Absorption Case

Station	Latitude	Longitude	Modeled BC in Rain, ng/g	Measured BC in Rain, ng/g	Period
Seattle	37°36′N	122°18′W	56–61	60 (28–130)[a]	Dec.–Jan.
North Sweden	66°N	20°E	6–15	172 (30–700)[a]	April–Aug.
South Sweden	60°N	16°E	11–42	193 (20–600)[a]	April–Aug.
Mace Head	53°18′N	9°54′W	5–8	31 (9–94)[b]	Oct.–Nov.
Gif sur Yvette	49°N	2°E	65–88	333 (27–1348)[b]	year
Enyele, Congo	2°29′N	18°06′E	30–160	155 (75–258)[b]	Nov.–March
Enyele, Congo	2°29′N	18°06′E	19–90	45 (11–75)[b]	May–Oct.
Lamto, Ivory Coast	8°N	5°W	10–101	69 (20–192)[b]	June–Oct.
Halifax, Nova Scotia	44°23′N	63°22′W	9–14	4 (0–11)[c]	Jan.–March

[a] *Ogren et al.* [1984].
[b] *Ducret and Cachier* [1992].
[c] *Chylek et al.* [1999].

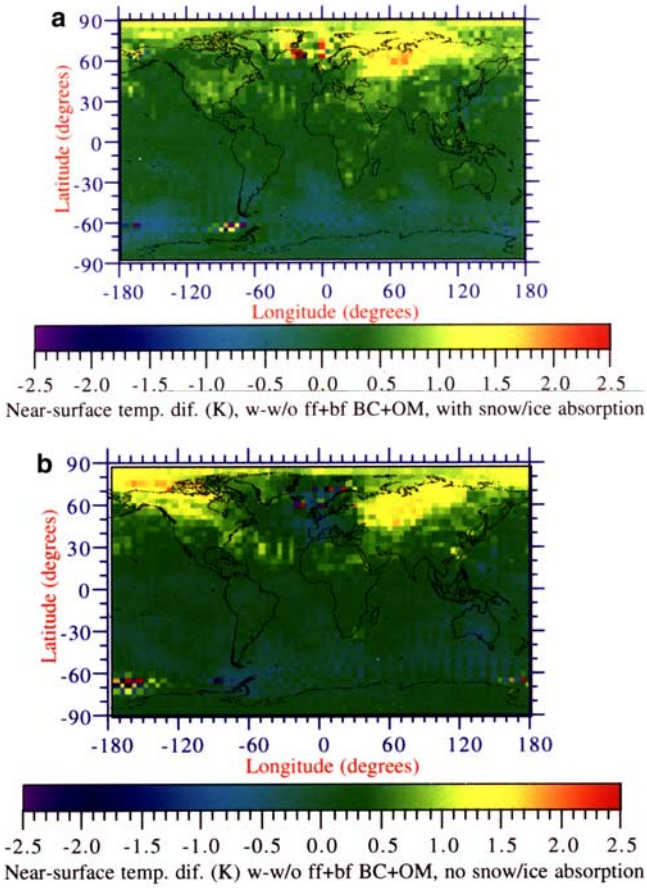

Figure 3. Ten-year average temperature difference due to the climate response of ff+bf BC+OM emission when absorption by BC inclusions in snow and sea ice (a) was accounted for ("baseline absorption" minus "sensitivity absorption" cases) and (b) was not accounted for ("baseline no absorption" minus "sensitivity no absorption" cases).

scribed change in albedo triggered by BC in snow and sea ice of about +0.17 K. Although the sign of the effect is consistent in both studies and intuitive, the magnitudes in both cases are still uncertain because of uncertainties in model physical processes, emission data, and treatment of feedbacks. Additional short-term simulations here found that variations in initial conditions resulted in modeled variations in the effects of BC absorption in snow and sea ice ranging from +0.03 to +0.11 K.

[57] The overall warming effect of ff+bf BC+OM found here (+0.27 K averaged over 10 years) is somewhat larger than that of *Hansen and Nazarenko* [2003] (+0.2 K) although their value lies within the range of values (+0.15 to +0.5 K) given by *Jacobson* [2002a]. Differences in the effects of BC on snow and sea ice undoubtedly arise because of differences in the methods of calculation, discussed in section 1, and differences in emission. Nevertheless, both studies support the contention that anthropogenic soot has an important climate impact.

[58] Figure 7 shows the modeled difference in surface albedo when ff+bf BC+OM emission was and was not included, respectively, and BC absorption in snow/sea ice was included in both cases. Albedo changes were due not only to BC inclusions in snow and sea ice but also to feedbacks of atmospheric BC to the presence of snow and sea ice. The figure shows albedo reductions, typically <3%, over most high-latitude areas in the Northern Hemisphere where BC deposition to snow and sea ice were expected. The Northern Hemisphere and globally averaged reductions were 1% and 0.4%, respectively. The largest decrease occurred over the Greenland Sea, where sea ice and snow over sea ice were modeled to be present much of the time. Northwestern Europe is a natural source region of BC to this region. It is possible that the large effect over the Greenland Sea was due to slight differences in snowfall when BC was present versus absent. Since snow thickness over sea ice is generally small, small changes in snow thickness can feed back strongly to radiative transfer since the albedo of sea ice, which lies below snow, is lower than is that of snow. However, because the albedo did not change so much in the "no-absorption" simulations when BC was present versus absent, the effect was most likely due to modeled effects of BC, not change in snowfall, on albedo.

[59] A slight increase in albedo occurred in the Southern Hemisphere near the edge of Antarctic sea ice due to a small increase in sea ice resulting from feedbacks of BC to large-scale meteorology (e.g., Figure 4). The globally averaged change in albedo here (−0.4%) is relatively consistent with the expected change in albedo from theory (section 5) when 5 ng/g of BC, the globally averaged BC in snow and sea ice calculated here, is present. However, the albedo change found here accounts for changes in snow and sea ice presence due to the climate response of BC as well as to changes due to BC absorption in snow and sea ice.

[60] Figure 8 shows the modeled versus measured zonally and 10-year-averaged December-January-February (DJF) albedo, integrated over the solar spectrum, from the baseline absorption simulation. DJF was chosen because the albedo is high in the Northern Hemisphere, where substantial BC is

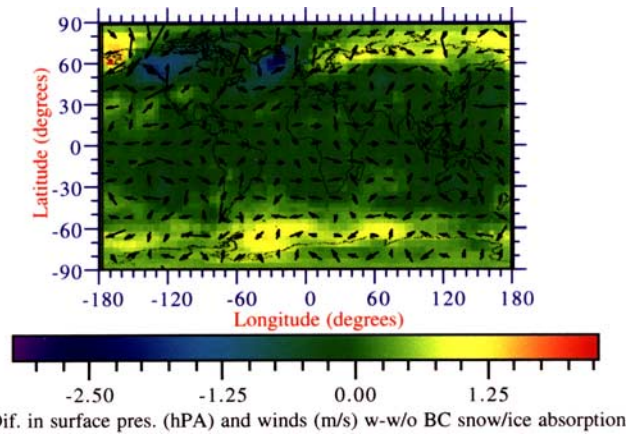

Figure 4. Ten-year average near-surface pressure differences (color) and wind differences (vectors) due to absorption by BC inclusions in snow and sea ice. This figure is the difference between the simulations in which snow and sea ice absorption were and were not included, respectively, but where ff+bf BC+OM emission was included in both simulations ("baseline absorption" minus "baseline no absorption" cases). The longest wind vector is 1.61 m/s.

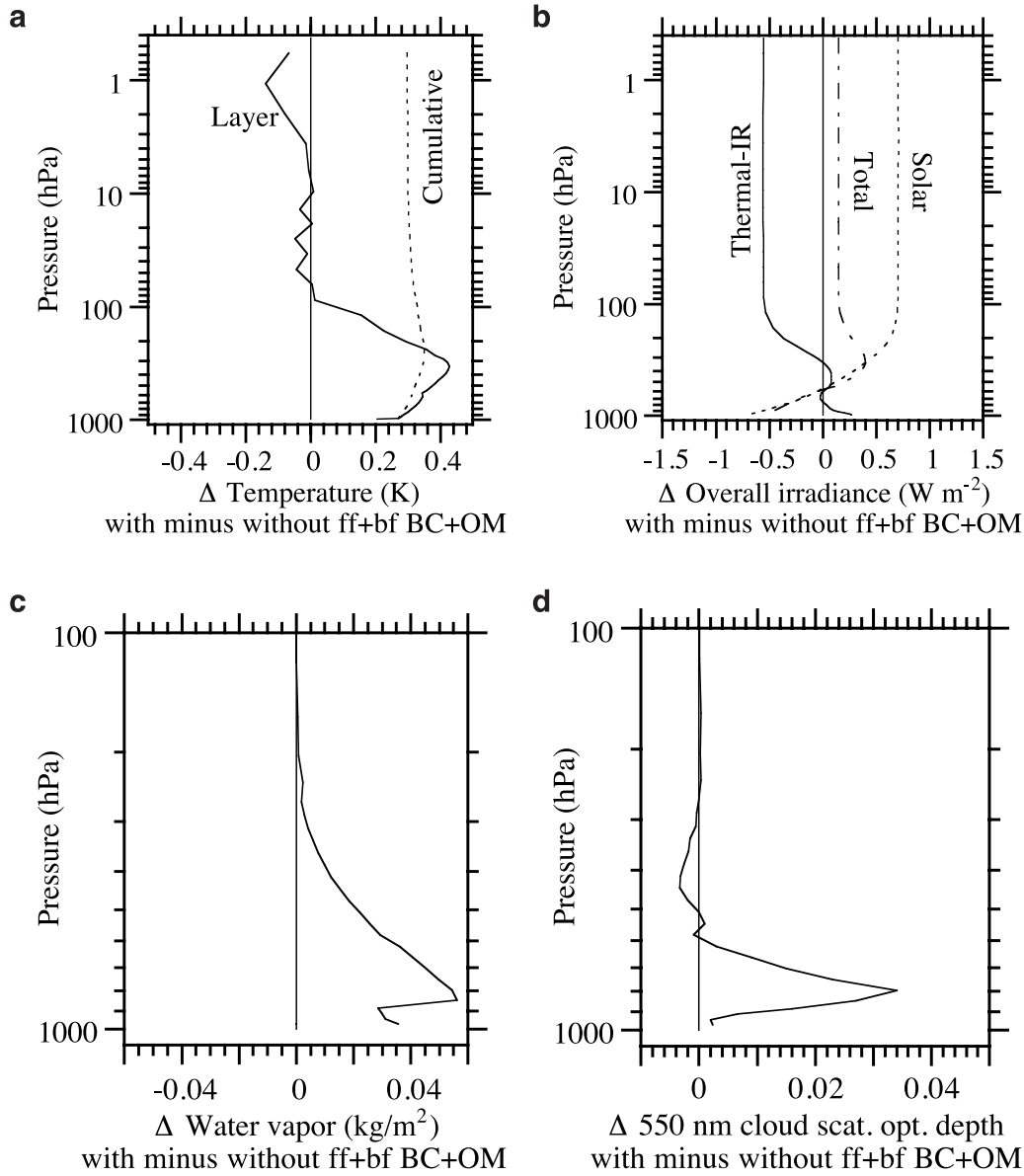

Figure 5. (a) Vertical profile of 10-year and globally averaged layer and cumulative temperature difference due to the climate response of ff+bf. BC+OM emission when the effect on snow and sea ice albedo of absorption by BC inclusions in snow and sea ice was included ("baseline absorption" minus "sensitivity absorption" cases). Please see the text for definitions of layer and cumulative temperature. (b) Same as Figure 5a but for the difference in net downward minus upward solar, thermal-IR, and total irradiance. (c) Same as Figure 5a but for the difference in water vapor. (d) Same as Figure 5a but for the difference in cloud-scattering optical depth at 550 nm. (e) Difference in modeled albedo when 25 ng/g is added to snow at a grain radius of 60 μm minus the difference when 25 ng/g is added to snow at a grain radius of 150 μm.

present, during these months. Two modeled values are shown: one with wavelength-dependent albedo specified as a function of time-dependent modeled land cover; the second with wavelength-dependent albedo predicted by the radiative transfer code, as described in section 4. The radiative transfer calculation always increased (when snow or sea ice was present) or caused no change in (all other cases) the surface albedo relative to the specified albedo because, in the presence of snow or sea ice, the Mie-derived backscattering for spherical particles, integrated over the depth of snow, was higher than the backscattering predicted by the specified albedo. The radiative transfer calculation improved the fit to the measurement in the Northern Hemisphere for DJF.

[61] Figure 9 shows the 10-year-averaged difference in the modeled surface solar radiation due to including versus excluding ff+bf BC+OM emission in the absorption case. The maximum increase in surface radiation occurred over the Greenland Sea, where the maximum decrease in surface albedo occurred because of BC absorption. Solar radiation

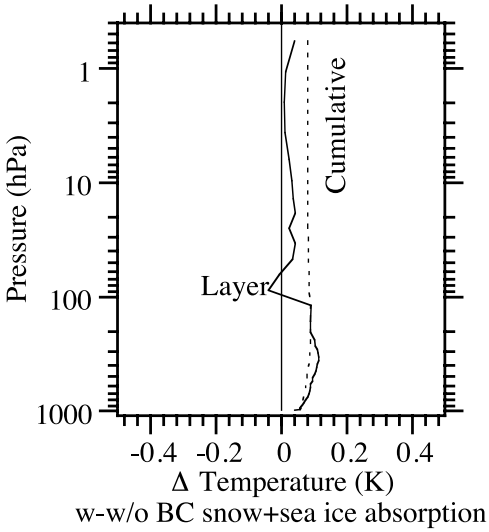

Figure 6. Same as Figure 5a, but due to the climate response of absorption by BC inclusions and sea ice only when ff+bf BC+OM emission was the same in both cases ("baseline absorption" minus "baseline no absorption" cases).

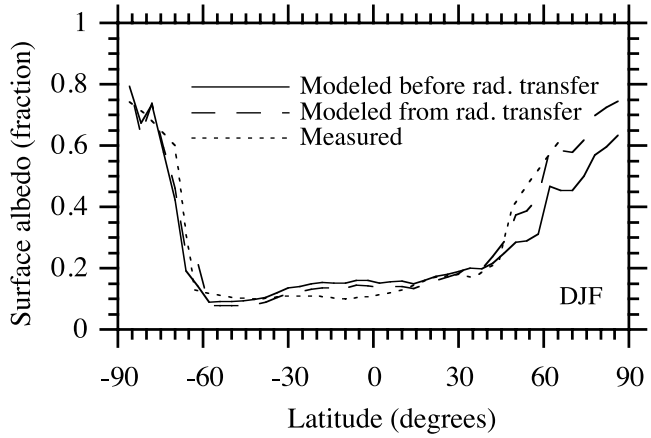

Figure 8. Ten-year zonally averaged modeled (from the "baseline absorption" simulation) versus measured [from *Kiehl et al.*, 1998] surface albedo (integrated over the solar spectrum) for December-January-February (DJF). "Modeled before rad. transfer" means the time-dependent model calculation was based on specified wavelength-dependent albedos applied to current modeled land covers (including snow, snow over sea ice, sea ice over water, water, bare soil with different water contents, soil with vegetation, vegetation with snow, rooftops, road surfaces, and as a function of zenith angle). "Modeled from rad. transfer" means from a radiative transfer calculation in each column of the 3-D model in which the bottom layer was a thin snow or sea ice layer containing BC, whose concentration was predicted over time.

also increased over much of northern Russia. Changes in surface solar radiation in the tropics were likely due to feedbacks of atmospheric BC to large-scale meteorology, which fed back to cloud cover. Regions in the tropics of decreased solar radiation corresponded to regions of increased cloud optical depth and vice versa (figure not shown).

[62] Figure 10 compares the time-dependent change in temperature due to eliminating ff+bf BC+OM (from the absorption case) with those obtained from reducing CH_4 and CO_2 emission (with three possible lifetimes in the CO_2 case). The three curves shown for CO_2 almost certainly capture the entire range of the CO_2 climate response. The CH_4 curve is the same as that given by *Jacobson* [2002a, Figure 1], but the CO_2 curves differ, as described by M. Z. Jacobson (Updates to "Control of fossil-fuel black carbon plus organic matter, possibly the most effective method of slowing global warming," http://www.stanford.edu/group/efmh/fossil/fossil.html, 2004). The ff+bf BC+OM curve was obtained from the 10 years of results from the present study. The value after 10 years was held constant at

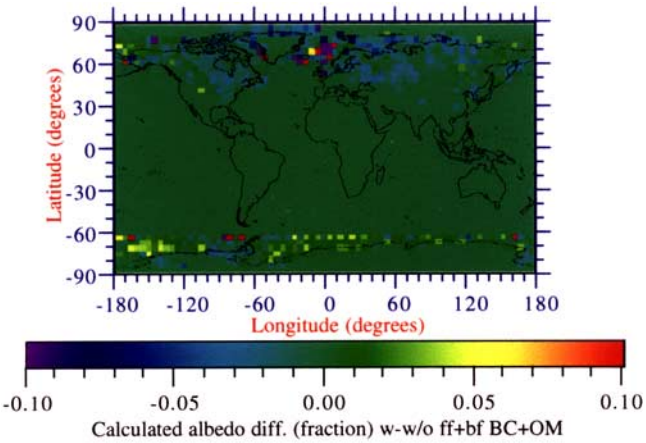

Figure 7. Ten-year-averaged difference in modeled (with the radiative transfer solution) surface albedo (fraction) when ff+bf BC+OM emission was versus was not included in the calculation ("baseline absorption" minus "sensitivity absorption" cases).

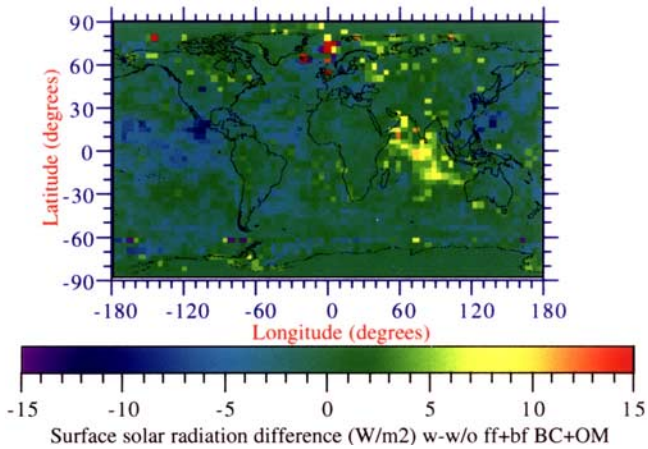

Figure 9. Ten-year-averaged difference in modeled downward surface solar irradiance (W/m^2) when ff+bf BC+OM emission was versus was not included in the calculation ("baseline absorption" minus "sensitivity absorption" cases).

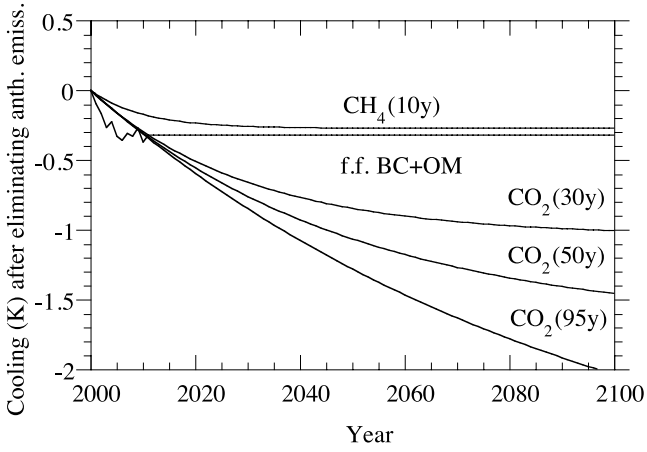

Figure 10. Comparison of time-dependent change in globally averaged near-surface temperature due to eliminating all anthropogenic emissions of each CO_2, CH_4, and ff+bf BC+OM. The CH_4 curve was obtained from *Jacobson* [2002a, Figure 1]. The CO_2 curves were obtained from M. Z. Jacobson (Updates to "Control of fossil-fuel black carbon plus organic matter, possibly the most effective method of slowing global warming," http://www.stanford. edu/group/efmh/fossil/fossil.html, 2004). The ff+bf BC+OM curve was obtained from the 10 years of results from the present study ("baseline absorption" minus "sensitivity absorption" cases). The value after 10 years was held constant at −0.32 K, the average of the last 3 years.

−0.32 K, the average of the last 3 years. The cooling in year 10 (−0.36 K) and the average cooling in the last 3 years (−0.32 K) were well within the uncertainty range (−0.15 to −0.5 K) of the cooling of −0.35 K found after 5 years given by *Jacobson* [2002a]. The 10-year average near-surface cooling found here was −0.27 K, which compares with a 5-year average given by *Jacobson* [2002a] of −0.3 K. The 10-year average ground cooling here was −0.2 K. Figure 10 suggests that control of ff+bf BC+OM may still be the most effective method of slowing global warming for a specific period (∼10 years). Controlling CO_2 is still more critical in the long term since it causes most warming and has a longer lifetime than does BC.

7. Conclusions

[63] A global model was modified to account for the effect of BC inclusions in snow and sea ice on albedos, emissivities, and temperatures. Spectral albedos in the model were predicted as the upward divided by downward irradiance at the top of the bottom layer of a column radiative transfer calculation. Emissivities were calculated from albedos. It was found that BC absorption in snow and sea ice increased globally averaged near-surface temperatures (over the 10-year simulation) by ∼0.06 K. The net 10-year average near-surface global warming due to ff+bf BC+OM, accounting for this absorption, was +0.27 K (the value in the tenth year was +0.36 K and in the last 3 years was +0.32 K). These values compare with the 5-year average from *Jacobson* [2002a] of +0.3 K and fifth-year value of +0.35 K. Much of the difference between the results can be attributed to a lower BC emission inventory used here, offset in part by treatment of BC absorption in sea ice and snow. The result here supports the previous findings that control of anthropogenic BC+OM, simultaneously with control of CO_2, may be an effective method of slowing global warming for a specific period. In this study, BC was calculated to reduce global snow and sea ice albedo by ∼0.4% in the global average and 1% in the Northern Hemisphere. The globally averaged modeled BC concentration in snow and sea ice was ∼5 ng/g; that in rainfall was ∼22 ng/g. About 98% of BC removal from the atmosphere was due to precipitation; the rest, to dry deposition.

[64] **Acknowledgments.** This work was supported by the NASA Earth Sciences Program, the Environmental Protection Agency Office of Air Quality Planning and Standards, and the National Science Foundation Atmospheric Chemistry Division (ATM 0101596).

References

Ackerman, T. P., and O. B. Toon (1981), Absorption of visible radiation in atmosphere containing mixtures of absorbing and nonabsorbing particles, *Appl. Opt.*, *20*, 3661–3667.

Aoki, T., T. Aoki, M. Fukabori, A. Hachikubo, Y. Tachibana, and F. Nishio (2000), Effects of snow physical parameters on spectral albedo and bi-directional reflectance of snow surface, *J. Geophys. Res.*, *105*, 10,219–10,236.

Arakawa, A., and V. R. Lamb (1981), A potential enstrophy and energy conserving scheme for the shallow water equations, *Mon. Weather Rev.*, *109*, 18–36.

Bohren, C. F. (1986), Applicability of effective-medium theories to problems of scattering and absorption by nonhomogeneous atmospheric particles, *J. Atmos. Sci.*, *43*, 468–475.

Bond, T. C., D. G. Streets, K. F. Yarber, S. M. Nelson, J. Woo, and Z. Klimont (2004), A technology-based global inventory of black and organic carbon emissions from combustion, *J. Geophys. Res.*, *109*, D14203, doi:10.1029/2003JD003697.

Chylek, P., V. Ramaswamy, and V. Srivastava (1983), Albedo of soot-contaminated snow, *J. Geophys. Res.*, *88*, 10,837–10,843.

Chylek, P., V. Srivastava, L. Cahenzli, R. G. Pinnick, R. L. Dod, T. Novakov, T. L. Cook, and B. D. Hinds (1987), Aerosol and graphitic carbon content of snow, *J. Geophys. Res.*, *92*, 9801–9809.

Chylek, P., V. Srivastava, R. G. Pinnick, and R. T. Wang (1988), Scattering of electromagnetic waves by composite spherical particles: Experiment and effective medium approximations, *Appl. Opt.*, *27*, 2396–2404.

Chylek, P., G. Videen, D. Ngo, R. G. Pinnick, and J. D. Klett (1995), Effect of black carbon on the optical properties and climate forcing of sulfate aerosols, *J. Geophys. Res.*, *100*, 16,325–16,332.

Chylek, P., L. Kou, B. Johnson, F. Boudala, and G. Lesins (1999), Black carbon concentrations in precipitation and near surface air in and near Halifax, Nova Scotia, *Atmos. Environ.*, *33*, 2269–2277.

Clark, R. N., and P. G. Lucey (1984), Spectral properties of ice-particulate mixtures and implications for remote sensing: 1. Intimate mixtures, *J. Geophys. Res.*, *89*, 6341–6348.

Clarke, A. D., and K. J. Noone (1985), Soot in the Arctic snowpack: A cause for perturbations in radiative transfer, *Atmos. Environ.*, *19*, 2045–2053.

Conway, H., A. Gades, and C. F. Raymond (1996), Albedo of dirty snow during conditions of melt, *Water Resour. Res.*, *32*, 1713–1718.

Cooke, W. F., and J. J. N. Wilson (1996), A global black carbon aerosol model, *J. Geophys. Res.*, *101*, 19,395–19,409.

Cooke, W. F., C. Liousse, H. Cachier, and J. Feichter (1999), Construction of a 1° × 1° fossil fuel emission data set for carbonaceous aerosol and implementation and radiative impact in the ECHAM4 model, *J. Geophys. Res.*, *104*, 22,137–22,162.

Davidson, C. I., S. Santhanam, R. C. Fortmann, and M. P. Olson (1985), Atmospheric transport and deposition of trace elements onto the Greenland ice sheet, *Atmos. Environ.*, *19*, 2065–2081.

Ding, P., and D. A. Randall (1998), A cumulus parameterization with multiple cloud-base levels, *J. Geophys. Res.*, *103*, 11,341–11,353.

Ducret, J., and H. Cachier (1992), Particulate carbon content in rain at various temperature and tropical locations, *J. Atmos. Chem.*, *15*, 55–67.

Fuller, K. A., W. C. Malm, and S. M. Kreidenweis (1999), Effects of mixing on extinction by carbonaceous particles, *J. Geophys. Res.*, *104*, 15,941–15,954.

Grenfell, T. C., S. G. Warren, and P. C. Mullen (1994), Reflection of solar radiation by the Antarctic snow surface at ultraviolet, visible, and near-infrared wavelengths, *J. Geophys. Res.*, *99*, 18,669–18,684.

Grenfell, T. C., B. Light, and M. Sturm (2002), Spatial distribution and radiative effects of soot in the snow and sea ice during the SHEBA experiment, *J. Geophys. Res.*, *107*(C10), 8032, doi:10.1029/2000JC000414.

Gribbon, P. W. F. (1979), Cryoconite holes on Sermikavsak, West Greenland, *J. Glaciol.*, *22*, 177–181.

Hansen, J., and L. Nazarenko (2003), Soot climate forcing via snow and ice albedos, *Proc. Natl. Acad. Sci. U. S. A.*, *101*(2), 423–428, doi:10.1073/pnas.2237157100.

Higuchi, K., and A. Nagoshi (1977), Effect of particulate matter in surface snow layers on the albedo of perennial snow patches, *IAHS AISH Publ.*, *118*, 95–97.

Jacobson, M. Z. (1997a), Development and application of a new air pollution modeling system. II: Aerosol module structure and design, *Atmos. Environ.*, *31*, 131–144.

Jacobson, M. Z. (1997b), Development and application of a new air pollution modeling system, III: Aerosol-phase simulations, *Atmos. Environ.*, *31*, 587–608.

Jacobson, M. Z. (1999), *Fundamentals of Atmospheric Modeling*, Cambridge Univ. Press, New York.

Jacobson, M. Z. (2000), A physically-based treatment of elemental carbon optics: Implications for global direct forcing of aerosols, *Geophys. Res. Lett.*, *27*, 217–220.

Jacobson, M. Z. (2001a), Strong radiative heating due to the mixing state of black carbon in atmospheric aerosols, *Nature*, *409*, 695–697.

Jacobson, M. Z. (2001b), GATOR-GCMM: A global- through urban-scale air pollution and weather forecast model: 1. Model design and treatment of subgrid soil, vegetation, roads, rooftops, water, sea ice, and snow, *J. Geophys. Res.*, *106*, 5385–5402.

Jacobson, M. Z. (2001c), GATOR-GCMM: 2. A study of daytime and nighttime ozone layers aloft, ozone in national parks, and weather during the SARMAP field campaign, *J. Geophys. Res.*, *106*, 5403–5420.

Jacobson, M. Z. (2002a), Control of fossil-fuel particulate black carbon plus organic matter, possibly the most effective method of slowing global warming, *J. Geophys. Res.*, *107*(D19), 4410, doi:10.1029/2001JD001376.

Jacobson, M. Z. (2002b), Analysis of aerosol interactions with numerical techniques for solving coagulation, nucleation, condensation, dissolution, and reversible chemistry among multiple size distributions, *J. Geophys. Res.*, *107*(D19), 4366, doi:10.1029/2001JD002044.

Jacobson, M. Z. (2003), Development of mixed-phase clouds from multiple aerosol size distributions and the effect of the clouds on aerosol removal, *J. Geophys. Res.*, *108*(D8), 4245, doi:10.1029/2002JD002691.

Jacobson, M. Z. (2004), A refined method of parameterizing absorption coefficients among multiple gases simultaneously from line-by-line data, *J. Atmos. Sci.*, in press.

Jacobson, M. Z., J. H. Seinfeld, G. R. Carmichael, and D. G. Streets (2004), The effect on photochemical smog of converting the U.S. fleet of gasoline vehicles to modern diesel vehicles, *Geophys. Res. Lett.*, *31*, L02116, doi:10.1029/2003GL018448.

Kiehl, J. T., J. J. Hack, and J. W. Hurrell (1998), The energy budget of the NCAR Community Climate Model: CCM3, *J. Clim.*, *11*, 1151–1178.

Krekov, G. M. (1993), Models of atmospheric aerosols, in *Aerosol Effects on Climate*, edited by S. G. Jennings, pp. 9–72, Univ. of Ariz. Press, Tucson.

Lesins, G., P. Chylek, and U. Lohmann (2002), A study of internal and external mixing scenarios and its effect on aerosol optical properties and direct radiative forcing, *J. Geophys. Res.*, *107*(D10), 4094, doi:10.1029/2001JD000973.

Light, B., H. Eicken, G. A. Maykut, and T. C. Grenfell (1998), The effect of included particulates on the spectral albedo of sea ice, *J. Geophys. Res.*, *103*, 27,739–27,752.

Maricq, M., D. H. Podsiadlik, and R. E. Chase (2000), Size distributions of motor vehicle exhaust PM: A comparison between ELPI and SMPS measurements, *Aerosol Sci. Technol.*, *33*, 239–260.

Massom, R. A., et al. (2001), Snow on Antarctica sea ice, *Rev. Geophys.*, *39*, 413–445.

Mellor, G. L., and T. Yamada (1982), Development of a turbulence closure model for geophysical fluid problems, *Rev. Geophys.*, *20*, 851–875.

Nijssen, B., R. Schnur, and D. P. Lettenmaier (2001), Global retrospective estimation of soil moisture using the variable infiltration capacity land surface model, 1980–1993, *J. Clim.*, *14*, 1790–1808.

Noone, K. J., and A. D. Clarke (1988), Soot scavenging measurements in Arctic snowfall, *Atmos. Environ.*, *22*, 2773–2778.

Ogren, J. A., P. J. Groblicki, and R. J. Charlson (1984), Measurement of the removal rate of elemental carbon from the atmosphere, *Sci. Total Environ.*, *36*, 329–338.

Podgorny, I. A., and T. C. Grenfell (1996), Absorption of solar energy in a cryoconite hole, *Geophys. Res. Lett.*, *23*, 2465–2468.

Rhodes, J. J., R. L. Armstrong, and S. G. Warren (1987), Mode of formation of "ablation hollows" controlled by dirt content of snow, *J. Glaciol.*, *33*, 135–139.

Schnaiter, M., H. Horvath, O. Mohler, K.-H. Naumann, H. Saathoff, and O. W. Schock (2003), UV-VIS-NIR spectral optical properties of soot and soot-containing aerosols, *J. Aerosol Sci.*, *34*, 1421–1444.

Toon, O. B., and T. P. Ackerman (1981), Algorithms for the calculation of scattering by stratified spheres, *Appl. Opt.*, *20*, 3657–3660.

Toon, O. B., C. P. McKay, T. P. Ackerman, and K. Santhanam (1989), Rapid calculation of radiative heating rates and photodissociation rates in inhomogeneous multiple scattering atmospheres, *J. Geophys. Res.*, *94*, 16,287–16,301.

Turpin, B. J., and H.-J. Lim (2001), Species contributions to PM2.5 mass concentrations: Revisiting common assumptions for estimating organic mass, *Aerosol Sci. Technol.*, *35*, 602–610.

Twohy, C. H., A. D. Clarke, S. G. Warren, L. F. Radke, and R. J. Charlson (1989), Light-absorbing material extracted from cloud droplets and its effect on cloud albedo, *J. Geophys. Res.*, *94*, 8623–8631.

Vehkamaki, H., M. Kulmala, I. Napari, K. E. J. Lehtinen, C. Timmreck, M. Noppel, and A. Laaksonen (2002), An improved parameterization for sulfuric acid-water nucleation rates for tropospheric and stratospheric conditions, *J. Geophys. Res.*, *107*(D22), 4622, doi:10.1029/2002JD002184.

Vogelmann, A. M., A. Robock, and R. G. Ellingson (1988), Effects of dirty snow in nuclear winter simulations, *J. Geophys. Res.*, *93*, 5319–5332.

Walcek, C. J., and N. M. Aleksic (1998), A simple but accurate mass conservative, peak-preserving, mixing ratio bounded advection algorithm with FORTRAN code, *Atmos. Environ.*, *32*, 3863–3880.

Warren, S. G. (1982), Optical properties of snow, *Rev. Geophys.*, *20*, 67–89.

Warren, S. G. (1984), Impurities in snow: Effects on albedo and snowmelt, *Ann. Glaciol.*, *5*, 177–179.

Warren, S. G., and A. D. Clarke (1990), Soot in the atmosphere and snow surface of Antarctica, *J. Geophys. Res.*, *95*, 1811–1816.

Warren, S. G., and W. J. Wiscombe (1980), A model for the spectral albedo of snow. II: Snow containing atmospheric aerosols, *J. Atmos. Sci.*, *37*, 2734–2745.

Warren, S. G., and W. J. Wiscombe (1985), Dirty snow after nuclear war, *Nature*, *313*, 467–470.

Woo, M.-K., and M.-A. Dubreuil (1985), Empirical relationship between dust content and arctic snow albedo, *Cold Reg. Sci. Technol.*, *10*, 125–132.

Zeng, X., R. E. Dickinson, A. Walker, M. Shaikh, R. S. DeFries, and J. Qi (2000), Derivation and evaluation of global 1-km fractional vegetation cover data for land modeling, *J. Appl. Meteorol.*, *39*, 826–839.

M. Z. Jacobson, Department of Civil and Environmental Engineering, Stanford University, Terman Engineering Center, Room M-13, Stanford, CA 94305-4020, USA. (jacobson@stanford.edu)